Air-Stable Room-Temperature Mid-Infrared Photodetectors Based on hBN/Black Arsenic Phosphorus/hBN Heterostructures

Shaofan Yuan,[†] Chenfei Shen,[‡] Bingchen Deng,[†] Xiaolong Chen,[†] Qiushi Guo,[†] Yuqiang Ma,[○]
Ahmad Abbas,[○,∇,¶,#] Bilu Liu,[○,◇] Ralf Haiges,[◆] Claudia Ott,[§] Tom Nilges,[§] Kenji Watanabe,[∥]
Takashi Taniguchi,[∥] Ofer Sinai,[⊥] Doron Naveh,[⊥] Chongwu Zhou,*[,‡,○] and Fengnian Xia*[,†]

[†]Department of Electrical Engineering, Yale University, New Haven, Connecticut 06511, United States

[‡]Mork Family Department of Chemical Engineering and Materials Science, University of Southern California, Los Angeles, California 90089, United States

[○]Ming Hsieh Department of Electrical Engineering, University of Southern California, Los Angeles, California 90089, United States

[◆]Loker Hydrocarbon Research Institute and Department of Chemistry, University of Southern California, Los Angeles, California 90089, United States

[§]Department of Chemistry, Technical University Munich, Lichtenbergstr 4, Garching bei München 85748, Germany

[∥]National Institute for Materials Science, 1-1 Namiki, Tsukuba, 305-0044, Japan

[⊥]Faculty of Engineering and Bar-Ilan Institute for Nanotechnology and Advanced Materials, Bar-Ilan University, Ramat Gan 52900, Israel

S Supporting Information

ABSTRACT: Layered black phosphorus (BP) has attracted wide attention for mid-infrared photonics and high-speed electronics, due to its moderate band gap and high carrier mobility. However, its intrinsic band gap of around 0.33 electronvolt limits the operational wavelength range of BP photonic devices based on direct interband transitions to around 3.7 μm. In this work, we demonstrate that black arsenic phosphorus alloy (b-As$_x$P$_{1-x}$) formed by introducing arsenic into BP can significantly extend the operational wavelength

range of photonic devices. The as-fabricated b-As$_{0.83}$P$_{0.17}$ photodetector sandwiched within hexagonal boron nitride (hBN) shows peak extrinsic responsivity of 190, 16, and 1.2 mA/W at 3.4, 5.0, and 7.7 μm at room temperature, respectively. Moreover, the intrinsic photoconductive effect dominates the photocurrent generation mechanism due to the preservation of pristine properties of b-As$_{0.83}$P$_{0.17}$ by complete hBN encapsulation, and these b-As$_{0.83}$P$_{0.17}$ photodetectors exhibit negligible transport hysteresis. The broad and large photoresponsivity within mid-infrared resulting from the intrinsic photoconduction, together with the excellent long-term air stability, makes b-As$_{0.83}$P$_{0.17}$ alloy a promising alternative material for mid-infrared applications, such as free-space communication, infrared imaging, and biomedical sensing.

KEYWORDS: *Two-dimensional materials, black arsenic phosphorus, heterostructures, medium-wavelength infrared photodetector, photoconduction*
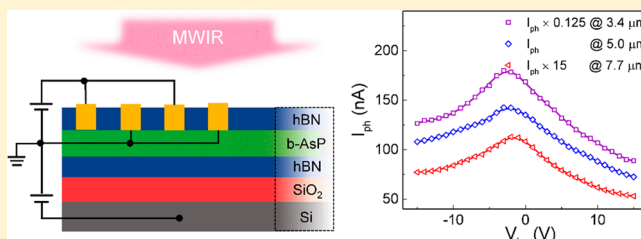
Semiconducting two-dimensional (2D) materials including various transition-metal dichalcogenides (TMDCs) and black phosphorus (BP)[1−4] have been extensively explored for photonic and electronic applications. The band gaps of most semiconducting TMDCs, such as molybdenum disulfide and tungsten diselenide, are close to or larger than 1 eV, which limits their optical applications to ultraviolet (UV), visible, and near-infrared (NIR) regions.[5] Black phosphorus, which has a band gap of 0.33 eV in thin film (>10 layers) or bulk form, can cover the short-wavelength infrared (SWIR) (0.9−2.5 μm) and part of the medium-wavelength infrared (MWIR) (3−5 μm).[6,7] Various studies on BP photodetection in UV,[8] visible,[9−11] NIR,[12] SWIR,[13,14] and MWIR (up to 3.4 μm)[15] were reported in the past few years, demonstrating the potential of BP in

wideband optoelectronic applications. Extending the operational range of BP photodetectors to even longer wavelength will significantly enhance its optical functionalities in various applications, such as thermal imaging and sensing. For example, blackbody radiation of objects with temperatures ranging from 300 to 1000 K has a peak intensity from 9.7 to 2.9 μm, which is crucial for industrial thermal imaging and infrared tracking.[16] Additionally, free-space optical communication at the first atmosphere window (3−5 μm) avoids significant signal attenuation for the wavelength-dependent nature of light scattering and at the same time keeps the unique advantages,

such as a higher data rate and enhanced transmission security.[17−19] Currently, the most commonly used material for photodetector applications in MWIR and long-wavelength infrared (LWIR) is $Hg_{1−x}Cd_xTe$ (MCT).[20] MCT is a popular choice due to its tunable band gap through the control of the composition and its high absorption in MWIR and LWIR.[20] However, besides its toxicity, its bulk nature makes its integration with other optical structures and components challenging.[21]

The black arsenic phosphorus was previously synthesized and its structural phase transition and superconductivity were studied.[22−25] Recently, one of the coauthors' group systematically synthesized and structurally characterized the layered black arsenic phosphorus (b-$As_xP_{1−x}$) alloy ($x \leq 0.83$) and demonstrated it still has a similar crystal structure to that of orthorhombic BP.[26] The synthesized b-$As_xP_{1−x}$ alloy has a tunable band gap down to ~0.12 eV, with an As concentration of 83%.[27] In a recent study, an IR detector based on the b-$As_xP_{1−x}$ alloy was reported with a decent responsivity for MWIR light.[28] In this device, the interplay among photovoltaic, photothermo-electric, and photogating effects leads to complicated photocurrent generation mechanisms at different incident power levels and operational speed. Moreover, the trap states on the b-$As_xP_{1−x}$/substrate interface can play an important role in such b-$As_xP_{1−x}$ photodetectors, and accordingly, the photoresponse time is long (0.5 ms), making its fast operation challenging. Another very recent work also reports b-$As_xP_{1−x}$ alloy based photodetectors.[29] In that work, the b-$As_{0.91}P_{0.09}$ photodetectors show very impressive responsivity and detectivity under mid-infrared excitation up to the wavelength of around 4.6 μm. The reported long carrier lifetime (above 1 μs) indicates that most likely the carrier trapping can also play a role in those devices.[29] In this study, we fully characterize the structural and optical properties of synthesized b-$As_{0.83}P_{0.17}$ and then utilize the narrow band gap of b-$As_{0.83}P_{0.17}$ to fabricate room temperature MWIR photodetectors operational in the intrinsic photoconduction regime, covering a wavelength range from 3.4 to 7.7 μm. In particular, to demonstrate the long-term stability of b-$As_{0.83}P_{0.17}$, which can be oxidized under exposure to air, we leverage the hexagonal boron nitride (hBN)/b-$As_{0.83}P_{0.17}$/hBN heterostructure for the effective protection. The as-fabricated photodetector shows an extrinsic responsivity of 190, 16, and 1.2 mA/W for 3.4, 5.0, and 7.7 μm incident light, respectively. We further study the photocurrent dependence on the applied gate (V_{bg}) and drain (V_{ds}) biases, from which we conclude that the photocurrent originates from the intrinsic photoconductive effect. Subsequent investigations of power and frequency dependence confirm the photoconduction mechanism. Moreover, due to the in-plane anisotropy in the crystal structure of b-$As_{0.83}P_{0.17}$,[27] a polarization-dependent photocurrent is observed. Our demonstration represents an important step for the future applications of b-$As_xP_{1−x}$ in a broad mid-infrared wavelength range, in particular for potential high-speed operations.

Results and Discussion. The b-$As_{0.83}P_{0.17}$ used for device demonstration in this work was prepared by an ampule synthesis method as demonstrated previously.[27] The stoichiometry of the b-$As_xP_{1−x}$ was controlled by the molar ratio of starting materials (gray arsenic/red phosphorus = 83:17). Details of the synthesis are presented in Methods.[30] The energy dispersive X-ray spectroscopy (EDS) spectrum of the synthesized b-$As_xP_{1−x}$ confirms that the compound is composed of ~83 atomic percent (at %) As and ~17 at % P.

(See the Supporting Information.) The powder X-ray diffraction (XRD) pattern of b-$As_{0.83}P_{0.17}$ is shown in Figure 1a. All diffraction peaks are indexed to corresponding planes. In b-$As_xP_{1−x}$, the interlayer distance is larger than that of gray arsenic at an arsenic concentration $\rho_{As} \approx 10\%$ and it increases monotonically as ρ_{As} further rises up to 83%,[26] which shows that the b-$As_xP_{1−x}$ crystal structure is very different from that of
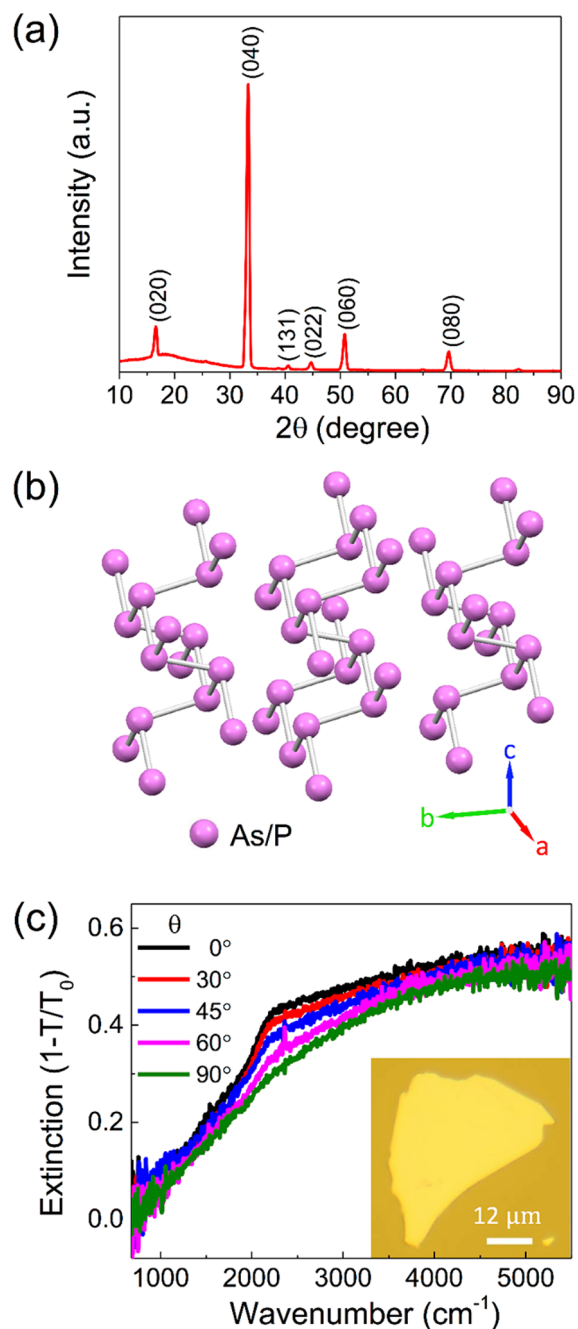

Figure 1. Crystal structure and infrared extinction characterizations. (a) X-ray diffraction pattern of the as-synthesized crystal with Miller indices labeled for peaks. The broad peak at 18° is from the Kapton tape, which is used to encapsulate the b-$As_{0.83}P_{0.17}$. (b) The orthorhombic puckered honeycomb crystal structure of b-$As_{0.83}P_{0.17}$ alloy. The lattice parameters, extracted from the X-ray diffraction profile, are a = 3.561(3) Å, b = 10.803(9) Å, and c = 4.493(4) Å. (c) Polarization-resolved IR extinction spectra of the b-$As_{0.83}P_{0.17}$ alloy. The optical image of the investigated flake is shown in the inset.
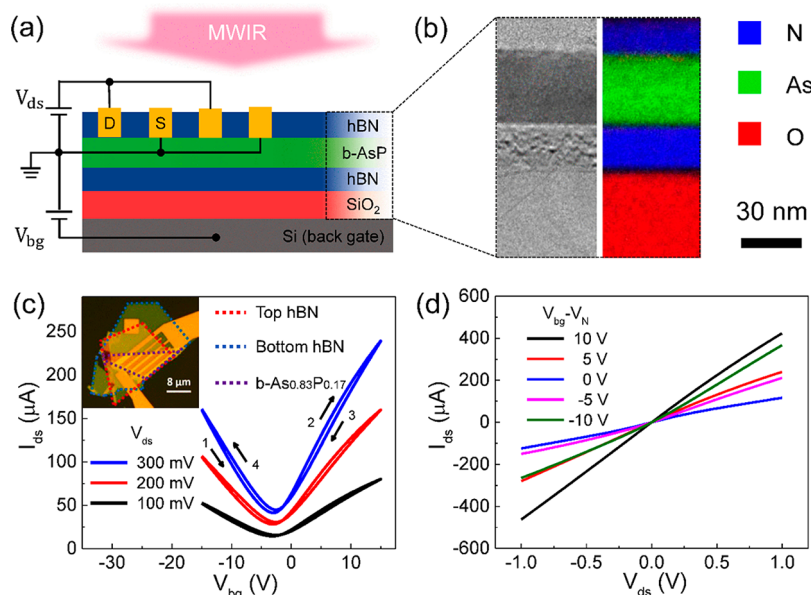
Figure 2. Device structure and electrical characterizations. (a) The cross-sectional schematic of the as-fabricated hBN/b-As$_{0.83}$P$_{0.17}$/hBN heterostructure photodetector. (b) Left: the cross-sectional view of the device by transmission electron microscope (TEM). Right: the elemental analysis mapping by electron energy loss spectroscopy (EELS). In the EELS mapping, red, blue, and green colors denote O, N, and As elements, respectively. Only part of the silicon oxide layer is shown. The encapsulated b-As$_{0.83}$P$_{0.17}$ layer is 37 nm, free from oxidation even several months after its fabrication. (c) Transfer characteristic of the as-fabricated phototransistor. The optical image of the as-fabricated device is shown in the inset. The gate bias was swept in both directions, with numbers denoting the sweeping sequence. The charge neutral point is at $V_{bg} = -3$ V, and the hysteresis of the transfer curve is small. (d) Output characteristics of the b-As$_{0.83}$P$_{0.17}$ phototransistor. The output curves were measured with different V_{bg}, and V_N represents the gate bias, at which the charge neutral point of the device is achieved ($V_N = -3$ V in this case).

gray arsenic. The diffraction pattern obtained in b-As$_{0.83}$P$_{0.17}$ here is consistent with the previous work,[26] and the interlayer distance is observably larger than that of gray arsenic. Detailed investigation of the crystal structure of b-As$_{0.83}$P$_{0.17}$ was done with single-crystal XRD. The single-crystal XRD analysis indicates that the b-As$_{0.83}$P$_{0.17}$ has an orthorhombic structure with a puckered honeycomb lattice as shown in Figure 1b.[27,30] (The atoms in Figure 1b represent either As or P.) The lattice parameters of the b-As$_{0.83}$P$_{0.17}$ are $a = 3.561(3)$ Å, $b = 10.803(9)$ Å, and $c = 4.493(4)$ Å, where a, b, and c are the lattice constants along the zigzag, stacking, and armchair direction. The details of the crystallographic data of b-As$_{0.83}$P$_{0.17}$ are provided in the Supporting Information.

Figure 1c shows the polarization-resolved infrared extinction spectra of a typical exfoliated b-As$_{0.83}$P$_{0.17}$ flake on the zinc sulfide (ZnS) substrate (shown in the inset), where T and T_0 are the optical transmission of the b-As$_{0.83}$P$_{0.17}$ flake on the ZnS substrate and the bare ZnS substrate, respectively. The measured extinction of the b-As$_{0.83}$P$_{0.17}$ flake shows an absorption edge around 1000 cm^{-1}, corresponding to a photon energy of 0.124 eV. The thickness of the investigated flake is measured to be 188 nm using an atomic force microscope (AFM), and the height profile of the flake edge can be found in the Supporting Information. We employ the Lambert−Beer's Law: $A(\omega) = 1 - e^{-\alpha(\omega)Z}$ to estimate the absorption constant $\alpha(\omega)$ of bulk b-As$_{0.83}$P$_{0.17}$, where $A(\omega)$ is the absorption, ω is the frequency of incident light, and Z is the flake thickness. In the calculation, we assume the absorption constant $\alpha(\omega)$ is the same for the bulk material $Z \gg 5$ nm.[31] The absorption constant can be slightly overestimated in this approach, considering the reflection at the b-As$_{0.83}$P$_{0.17}$ surface. (See the Supporting Information.) For incident light wavelength $\lambda = 3.4$ μm ($\nu = 2950$ cm^{-1}), the absorption constant α is calculated to

be 2.7×10^4 cm^{-1}, using the 48% absorption in the 188 nm-thick flake.

After fully characterizing b-As$_{0.83}$P$_{0.17}$ flakes, we fabricated photodetectors based on hBN/b-As$_{0.83}$P$_{0.17}$/hBN heterostructures. The bottom hBN flakes were first exfoliated on a silicon substrate (Si) covered by a 90 nm-thick silicon oxide layer (SiO$_2$), and then the substrate was annealed in an argon/hydrogen (Ar/H$_2$) atmosphere at 600 °C for 6 h to remove possible polymer residues in the exfoliation. The b-As$_{0.83}$P$_{0.17}$ flake and the top hBN were transferred onto the bottom hBN flakes subsequently using a polymer-free dry transfer method.[32] All transfer processes were performed in an argon-filled glovebox to minimize oxidation. After 6 h of annealing in Ar/H$_2$ atmosphere at 300 °C, the defined metal contact region was etched to expose b-As$_{0.83}$P$_{0.17}$ and then electrodes (3/47 nm Chromium/Gold) were deposited.[33] Details of fabrication can be found in Methods.

Similar to BP,[34,35] b-As$_x$P$_{1-x}$ can also be oxidized in air, which makes the naked devices unstable in the long run. The encapsulation provides reliable protection for the b-As$_{0.83}$P$_{0.17}$ alloy against the oxidation and degradation. Figure 2a shows the cross-sectional schematic of the hBN/b-As$_{0.83}$P$_{0.17}$/hBN heterostructure photodetector on a SiO$_2$/Si substrate. It is based on a field-effect transistor scheme with an interdigitated source and drain electrodes to maximize the photocurrent collection efficiency. The cross-sectional view of the device and the elemental analysis by transmission electron microscope (TEM) are shown in Figure 2b. The 37 nm-thick b-As$_{0.83}$P$_{0.17}$ is well preserved in hBN and free from oxidation several months after its fabrication as shown in the elemental analysis in Figure 2b. The relatively thick b-As$_{0.83}$P$_{0.17}$ flake is chosen to enhance the absorption of IR light. The thicknesses of the top and bottom

hBN layers are 20 and 22 nm, respectively, determined from the cross-sectional TEM image.

The transfer characteristics of the as-fabricated device are plotted in Figure 2c. The inset shows its optical image. The device exhibits a rather symmetrical ambipolar property compared to previous studies,[15,28] probably due to the hBN encapsulation, which leads to the preservation of the intrinsic properties of b-As$_{0.83}$P$_{0.17}$. When V_{bg} is swept in both directions, the encapsulated b-As$_{0.83}$P$_{0.17}$ transistors exhibit negligible hysteresis, due to the clean hBN/b-As$_{0.83}$P$_{0.17}$ interfaces. The electron and hole mobilities can be extracted using $\mu = \left(\frac{dI_{ds}}{dV_{bg}}\right)(L/W)(1/V_{ds}C_g)$, where I_{ds} is the drain current, C_g is the gate capacitance, and $L = 1.5$ μm and $W = 30$ μm are the length and the total width of the transistor channel. Here both the hBN and SiO$_2$ are taken into account for the gate capacitance calculation, with a relative dielectric constant of 3.1 and 3.9, respectively.[36] Based on this approach, the extracted effective electron and hole mobilities are about 83 and 79 cm^2/(V s), respectively. We note that the intrinsic carrier mobilities could be higher than the extracted effective mobilities above, which do not exclude the contribution of the contact resistance. Figure 2d shows the output curves of the as-fabricated device at various back gate biases. The near-linear relation between I_{ds} and V_{ds} indicates that the Ohmic contact is achieved between metal electrodes and b-As$_{0.83}$P$_{0.17}$. The slight asymmetry in the magnitude of drain currents at opposite V_{ds} biases is most likely caused by the doping difference ($V_{bg} - V_{ds}$) around the drain electrode, which has previously been observed in conventional metal oxide semiconductor (MOS) transistors.[37]

Then we characterized the photoresponse of b-As$_{0.83}$P$_{0.17}$ devices for MWIR light at 3.4, 5.0, and 7.7 μm. The incident IR light was mechanically chopped at a certain frequency (3 kHz, if not specified), and the alternating photocurrent (I_{ph}) at a corresponding frequency was acquired using a lock-in amplifier. Since b-As$_x$P$_{1-x}$ has intrinsic anisotropic optical properties, the photocurrent naturally depends on the incident light polarization. The polarization-dependent photocurrent was measured when the device was biased at the charge neutral point and $V_{ds} = 300$ mV. In Figure 3a, the photocurrent is plotted in a polar coordinate as a function of the polarization for 3.4, 5.0, and 7.7 μm incident light. The photocurrent anisotropy, defined as the photocurrent ratio along the armchair and zigzag directions, is ~12, 14, and 1.3 for 3.4, 5.0, and 7.7 μm lasers, respectively. We notice that the anisotropy of photocurrent is stronger than that observed in the infrared extinction curves as shown in Figure 1c. In infrared extinction spectra, a large area (~30 μm × 30 μm × 0.188 μm) flake was used to accommodate the incident light from Fourier transform infrared spectrometer (FTIR), while the device was fabricated on a much smaller flake (~8 μm × 8 μm × 0.037 μm). Accordingly, the measured anisotropy in extinction spectra is the average over a larger area, which can contain multiple crystalline domains. As a result, the infrared extinction spectra show much less anisotropy. The weak photocurrent and infrared extinction at the band edge may be due to the emergence of a new less anisotropic valence band at a high arsenic concentration, as suggested by the recent calculations based on the density function theory.[38]

The photocurrent dependence on V_{bg} was measured at a light polarization along the armchair direction.[27] For an incident laser with different photon energies, the photocurrent always
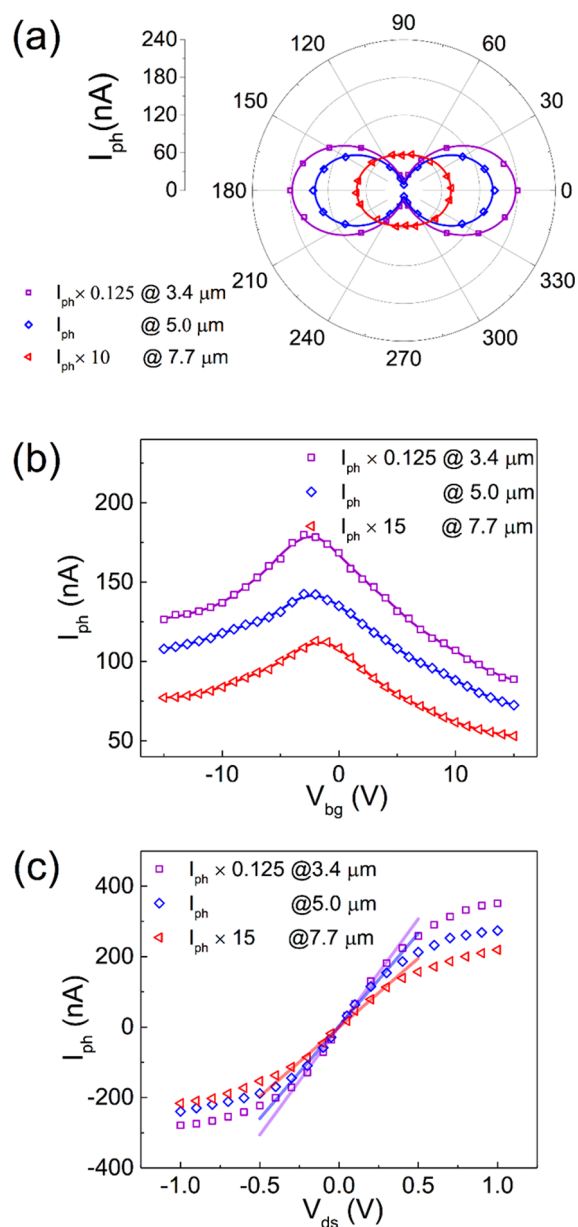

Figure 3. Photoresponse of hBN-encapsulated b-As$_{0.83}$P$_{0.17}$ phototransistor. (a) Polarization-resolved photocurrents of the b-As$_{0.83}$P$_{0.17}$ phototransistor for 3.4, 5.0, and 7.7 μm light excitation at $V_{ds} = 0.3$ V when the device is biased at a charge neutral point. (b) V_{bg} dependence of the photocurrent in the b-As$_{0.83}$P$_{0.17}$ phototransistor at $V_{ds} = 0.3$ V. (c) The photoresponse as a function of source-drain bias V_{ds}. In this measurement, the device works at a charge neutral point. Transparent colored lines are the linear fitting in the range of |V_{ds}| < 0.4 V. The photocurrent in panels b and c was measured when the polarization of incident light was aligned with the armchair direction.

peaks at the charge neutral point, as shown in Figure 3b. This is the typical feature of the photoconductive effect, since the higher doping away from the charge neutral point reduces the photocarrier lifetime, leading to the reduction in photocurrent.[39] At the charge neutral point, the photocurrent scales almost linearly with V_{ds} when |V_{ds}| < 0.4 V, as shown in Figure 3c. The saturation of the photocurrent at a large V_{ds} can be attributed to the Joule heating effect, which sets the limit of the internal amplification for the decreasing photocarrier lifetime at

a higher temperature.[40] The extrinsic responsivity is estimated using $R_{ex} = I_{ph}/(P_{in}\xi)$, where P_{in} is the power of incident light and ξ is the ratio of the incidence power on the device to the total incidence power, considering the Gaussian distribution of light intensity. (See the Methods for the calculation of ξ.) When the device is biased at $V_{ds} = 1$ V and $V_{bg} = -3$ V (corresponding to the charge neutrality point), the corresponding extrinsic responsivity for 3.4, 5.0, and 7.7 μm laser is calculated to be ~190, 16, and 1.2 mA/W, respectively.

To further elucidate the photocurrent generation mechanism, the power and frequency dependence of the photocurrent were also measured. As shown in Figure 4a, in our hBN/b-As$_{0.83}$P$_{0.17}$/hBN photodetectors, the photocurrent scales approximately linearly with input power. This is distinctively different from the previously demonstrated b-As$_{0.83}$P$_{0.17}$ photodetector,[28] which shows a sublinear power-dependent photocurrent. The decreasing responsivity at a higher intensity light in the previous work can be attributed to trap states on the b-As$_x$P$_{1-x}$/SiO$_2$ interface. At a higher illumination condition, surface trap states are densely occupied, leading to the saturation of the photogating effect and decreasing responsivity. In our device, the intrinsic photoconduction leads to a photocurrent linearly scaled with the input power, since more electron−hole pairs can be excited proportionally by a higher intensity light. Besides the distinguished power dependency, our hBN-encapsulated b-As$_{0.83}$P$_{0.17}$ MWIR photodetector also shows an excellent response speed. The photocurrent remains constant when the chopped frequency of incident light ranges from 1 to 10 kHz, which indicates that the 3 dB cutoff frequency of the device is well beyond 10 kHz (Figure 4b). Here we use the photocarrier lifetime to estimate the intrinsic 3 dB cutoff frequency of the device.[41] With the absorption constant $\alpha(\omega)$ calculated from the extinction spectra, we estimate the absorption (η) of the 37 nm-thick flake to be 12% at 3.4 μm using Lambert−Beer's Law. Then the product of internal quantum efficiency (IQE) and photoelectric current gain G at the charge neutral point and $V_{ds} = 1$ V is calculated, with IQE·$G = (R_{ex}/\eta)(E_{ph}/e)$, to be around 60%, where E_{ph} is the photon energy and e is the elementary charge. On the other hand, the transition time $\tau_{tr} = L^2/(\mu V_{ds})$ for electrons and holes is calculated to be 27 and 29 ps, respectively. Considering both carrier transition time and IQE·G, the photocarrier lifetime at the charge neutral point ($\tau_{life} = \tau_{tre}\tau_{trh}/(\tau_{trh} + \tau_{tre})$·IQE·$G$) is estimated to be around 8 ps, where $\tau_{tre/h}$ is the transition time for electrons or holes.[41] Here the estimated photocarrier lifetime in b-As$_{0.83}$P$_{0.17}$ is about an order of magnitude smaller than the previously measured value of ~100 ps in hBN covered BP using the time-resolved reflection measurements.[42] This is probably due to the lower quality of compound b-As$_{0.83}$P$_{0.17}$ and its smaller band gap. The compound nature of b-As$_{0.83}$P$_{0.17}$ can lead to a lower sample quality, which can result in an enhanced nonradiative recombination rate and reduced photocarrier lifetime. Moreover, its smaller band gap results in a higher intrinsic carrier density, which can lead to an enhanced recombination rate and hence reduced carrier lifetime.[43] However, it is much shorter than previously reported device response times (longer than 1 μs in refs 28 and 29) because the intrinsic photocarrier lifetime and device response time are two different physical quantities. The device response time in refs 28 and 29 is likely dominated by the lifetime of the trapped photocarriers at the band edge, which sometimes can be extremely long.[44] The calculated photocarrier lifetime in this work suggests a potential 3 dB cutoff frequency ($f_{3dB} = 1/$

Figure 4. Power and frequency dependence of the photocurrent and noise characteristics. (a) Photocurrent as a function of incident power at 3.4 μm when the device works at a charge neutral point and $V_{ds} = 0.3$ V. The laser polarization is aligned with the armchair direction. (b) Photoresponse as a function of the incident light intensity modulation frequency from 1 to 10 kHz, showing no sign of response roll-off. (c) Noise equivalent power at $V_{ds} = 1$ V for 3.4, 5.0, and 7.7 μm incident light when the device works at a charge neutral point and the light polarization is aligned with the armchair direction.

$(2\pi\tau_{life}))$ of the photoconductor at around 19 GHz. In terms of the photocurrent generation mechanism, the observed fast photoresponse also eliminates the probability of photogating effects in our hBN-encapsulated b-As$_{0.83}$P$_{0.17}$ photodetectors.[15]

Since the as-fabricated b-As$_{0.83}$P$_{0.17}$ photodetectors intrinsically operate at high frequencies, the frequency-independent shot noise and thermal noise play the major role in the
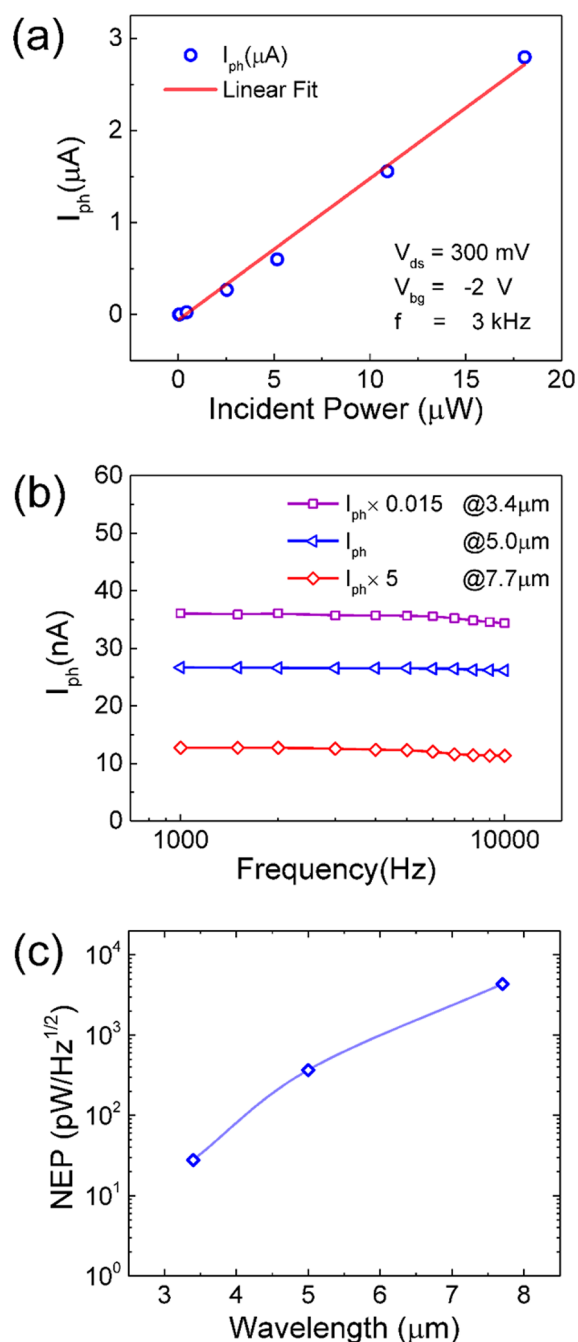
detection. The contribution from $1/f$ flicker noise is significant only at low operating frequencies (<10 kHz)[45] and, hence, is out of scope in this work. We estimated the detection noise and corresponding noise equivalent power (NEP) at high frequencies considering the shot noise, thermal noise, and generation-recombination noise in the device.[41] The current noise power spectral density function S_S of the shot noise, generated from the discrete nature of electrons, is given by $S_S = 2eI_{ds}$. For thermal noise, it originates from a random thermal motion of electrons and is expressed as $S_T = \frac{4kT}{R}$, where k is Boltzmann constant, T is the device working temperature, and R is the device resistance. The generation and recombination of photocarriers is another generation source of noise, but we estimate the generation-recombination noise, $S_{GR} = 4eI_{ph}(\tau_{life}/\tau_{tr})/(1 + (2\pi f \tau_{life})^2$,[41] to be smaller than the shot noise by more than one order and contributes little to the NEP in our case (Supporting Information). The noise measurement at a charge neutral point indicates that the $1/f$ noise is not significant at frequencies above 2 kHz, as shown in the Supporting Information. With considerations above, we estimate the noise current density ($\delta i = \sqrt{S_S + S_T}$) and the noise equivalent power (NEP = $\delta i / R_{ex}$) at $V_{ds} = 1$ V at charge neutral points for 3.4, 5.0, and 7.7 μm incident light when the light polarization is aligned along the armchair direction. The operating dark current is 117 μA. and the associated noise current density is 6.3 pA/Hz$^{1/2}$. Then we calculate the NEP of our photodetector to be 28, 370, and 4300 pW/Hz$^{1/2}$ for 3.4, 5.0, and 7.7 μm incident light as shown in Figure 4c. Compared with previous works on black arsenic phosphorus MWIR photodetectors (refs 28 and 29), our sandwiched b-As$_{0.83}$P$_{0.17}$ device is different in terms of the operational mechanism, dynamical range, and potential speed. The b-As$_x$P$_{1-x}$ FET photodetector reported in ref 28 has an impressive NEP ∼ 3 pW/Hz$^{1/2}$ at 3.4 μm, and the molybdenum disulfide/b-AsP heterostructure results in an even smaller NEP ∼ 0.2 pW/Hz$^{1/2}$ at 3.4 μm. In ref 29, the authors characterized the comprehensive spectral response of black arsenic phosphorus FET using the blackbody flood illumination. They reported an impressive peak detectivity of 2.4 × 10^{10} cm Hz$^{1/2}$W^{-1} at around 4.2 μm instead of the NEP. In this work, we calibrate the device responsivity at three typical mid-infrared wavelengths using the quantum cascade lasers and provide accurate measurement results especially at longer wavelengths. In both refs 28 and 29, the photogating induced gain is likely to play an important role for improved NEP and detectivity values.[15] Here our device operates in the intrinsic photoconduction regime due to the hBN encapsulation. As a result, although the NEP and detectivity of our devices are not as impressive as previously demonstrated values, our devices have a larger operational dynamical range and potentially much improved operational speed. The layered nature of b-As$_{0.83}$P$_{0.17}$ allows further integration with resonant microcavities or mid-infrared waveguide,[14,46] which is expected to further improve its responsivity and may ultimately be used in on-chip spectroscopy and free-space optical communications.

Conclusions. In conclusion, we investigate the structural and optical properties of the synthesized b-As$_{0.83}$P$_{0.17}$ and further demonstrate the MWIR photodetectors, which cover a broad mid-IR wavelength range from 3.4 to 7.7 μm. Most importantly, the hBN encapsulation provides long-term air stability for the device and eliminates trap states at the interfaces. In terms of the photocurrent generation mechanism, on the contrary to previously demonstrated BP and b-As$_x$P$_{1-x}$ photodetectors,[15,28,29] the b-As$_{0.83}$P$_{0.17}$ photodetectors demonstrated in this work operate in intrinsic photoconduction mode and exhibit extrinsic photoresponsivity of 190, 16, and 1.2 mA/ W for 3.4, 5.0, and 7.7 μm incident light, respectively. The 3 dB cutoff frequency for MWIR detection can potentially be as high as 19 GHz.

Methods. *Crystal Synthesis.* The b-As$_{0.83}$P$_{0.17}$ samples were prepared from a mixture of gray arsenic (Chempur, 99.9999%) and red phosphorus (Chempur, 99.999$^+$%) with a molar ratio of 83:17. Lead(II) iodide (PbI$_2$, 12 mg per 625 mg batch) was added as the mineralizing agent. The chemicals were enclosed in evacuated silica glass ampules during reaction (length 100 mm, inner diameter 10 mm). Synthesis was performed in a Nabertherm furnace (L3/11/P330). The samples were heated up to 550 °C within 8 h, held at this temperature for 24 h, and then cooled to room temperature within 20 h.

Crystal Characterization. Powder X-ray diffraction (XRD) was carried out on a Rigaku Ultima IV powder/thin-film diffractometer with a Cu Kα radiation source. The diffractometer consists of an APEX II CCD detector and an Oxford Cryosystems Cryostream 700 apparatus for the collection of data at low temperatures. The crystals were mounted in Cryo-Loops using Paratone oil. A complete hemisphere of data was scanned on Ω (0.5°) at a detector distance of 50 mm and a resolution of 512 × 512 pixels. A total of 2520 frames were collected. The frames were integrated using the SAINT algorithm[47] to produce the (hkl) data file. Data were corrected for absorption effects using the multiscan method (SADABS).[48] The structures were solved and refined on F^2 using the Bruker SHELXTL Software Package.[49,50] CCDC nos. 1582392 and 1582393 contain the supplementary crystallographic data for this paper. These data can be obtained free of charge from The Cambridge Crystallographic Data Centre (www.ccdc.cam.ac. uk). Energy dispersive X-ray spectroscopy (EDS) was conducted on the JEOL JSM-7001 system.

Device Fabrication. The bottom hBN thin film was exfoliated on a 90 nm SiO$_2$/Si substrate and was then annealed at 600 °C in argon/hydrogen (Ar/H$_2$) to eliminate the possible polymer contamination in the exfoliation. The b-As$_{0.83}$P$_{0.17}$ and top hBN thin film were exfoliated mechanically from bulk crystals on polydimethylsiloxane (PDMS), which is attached to a glass slide. Then the b-As$_{0.83}$P$_{0.17}$ and hBN thin film were transferred on the bottom hBN subsequently to form the heterostructures. All of the steps above except annealing were finished in the glovebox, in which the oxygen and water concentration is well below 1 ppm. The sandwich structure was annealed at 300 °C in an Ar/H$_2$ atmosphere to decrease possible polymer residues in the structure. Poly methyl methacrylate (PMMA) e-beam resist was spin coated on the chip, and electron-beam lithography was used to define metal electrodes. The top hBN in the defined region was etched with fluoroform/oxygen (CHF$_3$/O$_2$) in the Oxford Plasmalab 100 system to open the source-drain window and to make contact with the b-As$_{0.83}$P$_{0.17}$ below. Finally, chromium/gold (3/47 nm) was deposited to make electrodes using a Kurt J. Lesker thermal evaporator.

Transmission Electron Microscope Imaging. High-resolution TEM (HR-TEM) images were acquired using an FEI Tecnai F-30 instrument at a working voltage of 300 kV. The device cross-sectional lamella was prepared using a focused Ga-ion beam (FIB) in a FEI Helios DualBeam machine after the

thermal evaporation of 6−10 nm amorphous carbon on the sample for conductivity. During the transfer to HR-TEM, the lamella was exposed to air for less than 5 min. Elemental mapping of the cross section was acquired using electron energy loss spectroscopy (EELS) combined with a Gatan imaging filter (GIF), yielding energy-filtered TEM (EFTEM) images.

Transport Measurements. The transport characteristics were measured with an Agilent B1500A semiconductor parameter analyzer in a Lakeshore cryogenic probe station. All electrical measurements above were performed in a vacuum (10^{-5} Torr) at room temperature.

Photocurrent Measurements. MWIR photocurrent measurements were performed in an ambient condition. The output light from MIR lasers was coupled into a Fourier transform infrared spectrometer (FTIR) and then was focused onto the device using an integrated Hyperion 2000 microscope. A 15× zinc selenide (ZnSe) objective in the Hyperion microscope was used to focus the light. The total incident power was around 30, 50, and 100 μW for 3.4, 5.0, and 7.7 μm lasers, respectively. In the calculation of extrinsic responsivity, the active device area A_{device} is 45 μm^2, and the standard deviations in the Gaussian distributions are measured to be around 5.1, 7.2, and 14 μm for 3.4, 5.0, and 7.7 μm lasers, respectively. The ratio ξ (power on the device directly to the total incident power) is estimated to be 0.83, 0.60, and 0.20 for 3.4, 5.0, and 7.7 μm light.

Polarized Infrared Extinction Measurements. The infrared absorption measurements were also performed using the FTIR and Hyperion 2000 microscope discussed above. An infrared polarizer was used to control the polarization of the infrared light.

◼ ASSOCIATED CONTENT

Ⓢ Supporting Information

The Supporting Information is available free of charge on the ACS Publications website at DOI: 10.1021/acs.nanolett.8b00835.

> Elemental composition analysis of b-As$_{0.83}$P$_{0.17}$, crystallographic information on b-As$_{0.83}$P, thickness profile of the exfoliated b-As$_{0.83}$P$_{0.17}$ used for extinction measurements, reflection measurements of the b-As$_{0.83}$P$_{0.17}$ flake on a ZnS substrate, calculation of noise equivalent power (NEP), and noise current density measurements at a charge neutral point (PDF)

◼ AUTHOR INFORMATION

Corresponding Authors

*E-mail: chongwuz@usc.edu.
*E-mail: fengnian.xia@yale.edu.

ORCID 🆔

Chenfei Shen: 0000-0001-8635-3429
Bilu Liu: 0000-0002-7274-5752
Kenji Watanabe: 0000-0003-3701-8119
Doron Naveh: 0000-0003-1091-5661
Chongwu Zhou: 0000-0001-8448-8450
Fengnian Xia: 0000-0001-5176-368X

Present Addresses

▽Center of Excellence for Green Nanotechnologies, Joint Centers of Excellence Program, King Abdulaziz City for Science and Technology, P.O Box 6086, Riyadh 11442, Saudi Arabia

¶Department of Electrical and Computer Engineering, University of Jeddah, Dhahban 23881, Saudi Arabia
#Department of Electrical and Computer Engineering, King Abdulaziz University, Abdullah Sulayman Street, Jeddah 22254, Saudi Arabia
◇Tsinghua-Berkeley Shenzhen Institute (TBSI), Tsinghua University, Shenzhen, 518055, P.R. China

Author Contributions

The manuscript was written through contributions of all authors. S.Y. and C.S. contributed equally to this work.

Notes

The authors declare no competing financial interest.

◼ REFERENCES

(1) Li, L. K.; Yu, Y. J.; Ye, G. J.; Ge, Q. Q.; Ou, X. D.; Wu, H.; Feng, D. L.; Chen, X. H.; Zhang, Y. B. *Nat. Nanotechnol.* **2014**, *9*, 372−377.

(2) Xia, F. N.; Wang, H.; Jia, Y. C. *Nat. Commun.* **2014**, *5*, 4458.

(3) Liu, H.; Neal, A. T.; Zhu, Z.; Luo, Z.; Xu, X. F.; Tomanek, D.; Ye, P. D. D. *ACS Nano* **2014**, *8*, 4033−4041.

(4) Koenig, S. P.; Doganov, R. A.; Schmidt, H.; Neto, A. H. C.; Ozyilmaz, B. *Appl. Phys. Lett.* **2014**, *104*, 104.

(5) Wang, Q. H.; Kalantar-Zadeh, K.; Kis, A.; Coleman, J. N.; Strano, M. S. *Nat. Nanotechnol.* **2012**, *7*, 699−712.

(6) Li, L. K.; Kim, J.; Jin, C. H.; Ye, G. J.; Qiu, D. Y.; da Jornada, F. H.; Shi, Z. W.; Chen, L.; Zhang, Z. C.; Yang, F. Y.; et al. *Nat. Nanotechnol.* **2016**, *12*, 21−25.

(7) Rodin, A. S.; Carvalho, A.; Castro Neto, A. H. *Phys. Rev. Lett.* **2014**, *112*, 112.

(8) Wu, J.; Koon, G. K. W.; Xiang, D.; Han, C.; Toh, C. T.; Kulkarni, E. S.; Verzhbitskiy, I.; Carvalho, A.; Rodin, A. S.; Koenig, S. P.; et al. *ACS Nano* **2015**, *9*, 8070−8077.

(9) Huang, M. Q.; Wang, M. L.; Chen, C.; Ma, Z. W.; Li, X. F.; Han, J. B.; Wu, Y. Q. *Adv. Mater.* **2016**, *28*, 3481−3485.

(10) Buscema, M.; Groenendijk, D. J.; Steele, G. A.; van der Zant, H. S. J.; Castellanos-Gomez, A. *Nat. Commun.* **2014**, *5*, 4651.

(11) Miao, J. S.; Zhang, S. M.; Cai, L.; Wang, C. *Adv. Electron. Mater.* **2016**, *2*, 1500346.

(12) Buscema, M.; Groenendijk, D. J.; Blanter, S. I.; Steele, G. A.; van der Zant, H. S. J.; Castellanos-Gomez, A. *Nano Lett.* **2014**, *14*, 3347−3352.

(13) Engel, M.; Steiner, M.; Avouris, P. *Nano Lett.* **2014**, *14*, 6414−6417.

(14) Youngblood, N.; Chen, C.; Koester, S. J.; Li, M. *Nat. Photonics* **2015**, *9*, 247−252.

(15) Guo, Q. S.; Pospischil, A.; Bhuiyan, M.; Jiang, H.; Tian, H.; Farmer, D.; Deng, B. C.; Li, C.; Han, S. J.; Wang, H.; et al. *Nano Lett.* **2016**, *16*, 4648−4655.

(16) Luong, M. P. *Nucl. Eng. Des.* **1995**, *158*, 363−376.

(17) Majumdar, A. K. *Free-Space Laser Communications: Principles and Advances*; Springer: New York, 2008.

(18) Hranilovic, S. *Wireless Optical Communication Systems*; Springer: New York, 2005.

(19) Capasso, F.; Paiella, R.; Martini, R.; Colombelli, R.; Gmachl, C.; Myers, T. L.; Taubman, M. S.; Williams, R. M.; Bethea, C. G.; Unterrainer, K.; et al. *IEEE J. Quantum Electron.* **2002**, *38*, 511−532.

(20) Dhar, N. K.; Dat, R.; Sood, A. K. Advances in Infrared Detector Array Technology. In *Optoelectronics - Advanced Materials and Devices*; Pyshkin, S. L., Ballato, J. M., Eds.; InTech: Rijeka, 2013.

(21) Rogalski, A.; Adamiec, K.; Rutkowski, J. *Narrow-Gap Semiconductor Photodiodes*; SPIE Press: Bellingham, WA, 2000.

(22) Krebs, H.; Holz, W.; Worms, K. H. *Chem. Ber.* **1957**, *90*, 1031−1037.

(23) Smith, P. M.; Leadbetter, A. J.; Apling, A. J. *Philos. Mag.* **1975**, *31*, 57−64.

(24) Shirotani, I.; Kawamura, H.; Tsuburaya, K.; Tachikawa, K. *Jpn. J. Appl. Phys.* **1987**, *26*, 921.

(25) Shirotani, I.; Mikami, J.; Adachi, T.; Katayama, Y.; Tsuji, K.; Kawamura, H.; Shimomura, O.; Nakajima, T. *Phys. Rev. B: Condens. Matter Mater. Phys.* **1994**, *50*, 16274−16278.

(26) Osters, O.; Nilges, T.; Bachhuber, F.; Pielnhofer, F.; Weihrich, R.; Schoneich, M.; Schmidt, P. *Angew. Chem., Int. Ed.* **2012**, *51*, 2994−2997.

(27) Liu, B. L.; Kopf, M.; Abbas, A. N.; Wang, X. M.; Guo, Q. S.; Jia, Y. C.; Xia, F. N.; Weihrich, R.; Bachhuber, F.; Pielnhofer, F.; et al. *Adv. Mater.* **2015**, *27*, 4423−4429.

(28) Long, M.; Gao, A.; Wang, P.; Xia, H.; Ott, C.; Pan, C.; Fu, Y.; Liu, E.; Chen, X.; Lu, W.; et al. *Sci. Adv.* **2017**, *3*, e1700589.

(29) Amani, M.; Regan, E.; Bullock, J.; Ahn, G. H.; Javey, A. *ACS Nano* **2017**, *11*, 11724.

(30) Kopf, M.; Eckstein, N.; Pfister, D.; Grotz, C.; Kruger, I.; Greiwe, M.; Hansen, T.; Kohlmann, H.; Nilges, T. *J. Cryst. Growth* **2014**, *405*, 6−10.

(31) Fox, M. *Optical Properties of Solids*; Oxford University Press: New York, 2010.

(32) Castellanos-Gomez, A.; Buscema, M.; Molenaar, R.; Singh, V.; Janssen, L.; van der Zant, H. S. J.; Steele, G. A. *2D Mater.* **2014**, *1*, 011002.

(33) Chen, X. L.; Wu, Y. Y.; Wu, Z. F.; Han, Y.; Xu, S. G.; Wang, L.; Ye, W. G.; Han, T. Y.; He, Y. H.; Cai, Y.; et al. *Nat. Commun.* **2015**, *6*, 7315.

(34) Favron, A.; Gaufres, E.; Fossard, F.; Phaneuf-L'Heureux, A. L.; Tang, N. Y. W.; Levesque, P. L.; Loiseau, A.; Leonelli, R.; Francoeur, S.; Martel, R. *Nat. Mater.* **2015**, *14*, 826−832.

(35) Wood, J. D.; Wells, S. A.; Jariwala, D.; Chen, K. S.; Cho, E.; Sangwan, V. K.; Liu, X. L.; Lauhon, L. J.; Marks, T. J.; Hersam, M. C. *Nano Lett.* **2014**, *14*, 6964−6970.

(36) Kim, K. K.; Hsu, A.; Jia, X. T.; Kim, S. M.; Shi, Y. M.; Dresselhaus, M.; Palacios, T.; Kong, J. *ACS Nano* **2012**, *6*, 8583−8590.

(37) Muller, R. S.; Kamins, T. I. *Device Electronics for Integrated Circuits*; John Wiley & Sons: Hoboken, NJ, 2002.

(38) Zhu, Z.; Guan, J.; Tomanek, D. *Nano Lett.* **2015**, *15*, 6042−6046.

(39) Nelson, J. *The Physics of Solar Cells*; Imperial College Press: London, 2003.

(40) Freitag, M.; Low, T.; Xia, F. N.; Avouris, P. *Nat. Photonics* **2013**, *7*, 53−59.

(41) Chuang, S. L. *Physics of Photonic Devices*; John Wiley & Sons: Hoboken, NJ, 2009.

(42) He, J. Q.; He, D. W.; Wang, Y. S.; Cui, Q. N.; Bellus, M. Z.; Chiu, H. Y.; Zhao, H. *ACS Nano* **2015**, *9*, 6436−6442.

(43) Rockett, A. *The Materials Science of Semiconductors*; Springer: Boston, MA, 2008.

(44) Furchi, M. M.; Polyushkin, D. K.; Pospischil, A.; Mueller, T. *Nano Lett.* **2014**, *14*, 6165−6170.

(45) Haartman, M. V.; Östling, M. *Low-Frequency Noise in Advanced MOS Devices*; Springer: Dordrecht, The Netherlands, 2007.

(46) Unlu, M. S.; Strite, S. *J. Appl. Phys.* **1995**, *78*, 607−639.

(47) *SAINT*, V7.68A; Bruker AXS: Madison, WI, 2009.

(48) *SADABS*, V2008/1; Bruker AXS: Madison, WI, 2008.

(49) Sheldrick, G. *Acta Crystallogr., Sect. A: Found. Crystallogr.* **2008**, *64*, 112−122.

(50) *Bruker SHELXTL*, V2011.4−0; Bruker AXS: Madison, WI, 2008.